A modified Doyle-Fuller-Newman model enables the macroscale physical simulation of dual-ion batteries

Alessandro Innocenti [a,b], Isaac Álvarez Moisés [c], Jean-François Gohy [c], Stefano Passerini [a,b,d,*]

[a] *Helmholtz Institute Ulm (HIU) Electrochemical Energy Storage, Helmholtzstrasse 11, 89081, Ulm, Germany*
[b] *Karlsruhe Institute of Technology (KIT), P.O. Box 3640, 76021, Karlsruhe, Germany*
[c] *Institute of Condensed Matter and Nanoscience (IMCN), Université Catholique de Louvain, Place L. Pasteur 1, 1348, Louvain-la-Neuve, Belgium*
[d] *Department of Chemistry, Sapienza University of Rome, Piazzale A. Moro 5, 00185, Rome, Italy*

HIGHLIGHTS

- Physical model for dual-ion batteries.
- Simulations of electrolyte salt concentration variations during charge and discharge.
- Experimental validation of simulations with PTMA-lithium battery.
- Influence of the geometry and electrolyte salt concentration on dual-ion battery performance.
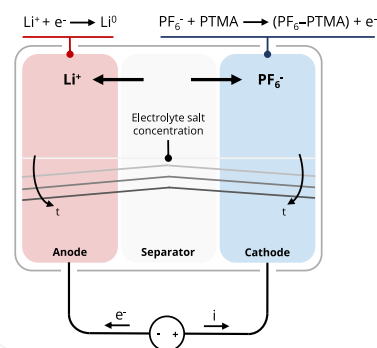
GRAPHICAL ABSTRACT

ARTICLE INFO

ABSTRACT

Dual-ion batteries are being considered a feasible approach for electrochemical energy storage. In this battery technology both cations and anions are involved in the redox reactions, respectively, at the anode and the cathode. However, the participation of both ions in the redox reactions means that enough salt must be added in the electrolyte to ensure proper battery functioning, which present a limiting factor in battery design. Herein, a modified version of the standard pseudo-2D Doyle-Fuller-Newman model is proposed to account for the different redox reactions that occur in dual-ion batteries and simulate the variation of average salt concentration in the electrolyte during charging and discharging. The model has been validated against galvanostatic cycling and electrochemical impedance spectroscopy experimental data from dual-ion batteries based on poly(2,2,6,6-tetramethyl-1-piperidinyloxy methacrylate) (PTMA). Such a model can be helpful to design practical dual-ion batteries that respect the constraints imposed by their working mechanism and maximize the obtainable capacity and energy density.

1. Introduction

Lithium-ion batteries are widely used for electric vehicles and stationary (renewable) energy storage, being currently the fastest growing electrochemical energy storage technology [1,2]. However, the ever-increasing demand for such batteries to electrify the transport and energy sectors and uncertainties in the supply of raw materials for their production have prompted the exploration of alternative and complementary solutions to the lithium-ion paradigm [3,4]. One promising direction is the development of dual-ion batteries, which involve both the electrolyte's cations and anions in the redox reactions for energy storage and release [5,6]. In a dual-ion battery, the cathode uptakes anions during charging while the anode stores cations. The ions are then released during discharging. The electrolyte plays a crucial role in this system, serving as the sole source of both anions and cations for the proper functioning of the dual-ion battery [7]. The main advantages of dual-ion batteries are the high average voltage reached by the cathode thanks to the interaction with the anions and the possibility of using cheap, sustainable, and widely available anion hosts as positive electrodes, like graphite or organic materials [8].

Nevertheless, the working principle of dual-ion batteries represents also their main drawback. The participation of the anions in the redox reaction means that there has always has to be enough salt in the electrolyte to allow the electrochemical reaction at the cathode to reach its full extent [7]. During the charge of the dual-ion battery, the salt concentration in the electrolyte decreases, due to the insertion of anions and cations respectively in the cathode and the anode. Vice versa, during discharge, the salt concentration increases due to the reversible de-insertion of the ions (Fig. 1). This cyclic behavior of the salt concentration during charge and discharge can be also found in lead-acid batteries, which are based on the reaction between negatively charged sulfate ions and lead/lead oxide electrodes [9]. In fact, the energy density of lead-acid batteries is mainly limited by the large amount of the concentrated sulfuric acid solution needed to avoid the salt depletion during the discharge of the battery.

The same line of reasoning applies then to dual-ion batteries, and their design has hence to consider a thick enough separation region between the electrodes and/or a highly concentrated electrolyte to ensure the presence of ions for the electrochemical reactions, both factors that decrease the energy density and increase the cost of a battery [10,11]. This is an additional limiting factor when compared for instance to lithium-ion batteries, where the salt concentration has local variations and gradients but then retains the same average value during operation [12]. In fact, in lithium-ion batteries, during charge Li-ions are de-inserted at the cathode and inserted in the anode, and vice versa during discharge (Fig. 1). Hence, the electrolyte is only a medium for the ions to travel between the electrodes, and a salt concentration of 1 M (1000 mol m^{-3}) is sufficient to ensure good ionic conductivity and to avoid local ion depletion at the electrode/electrolyte interface.

As dual-ion batteries transition from laboratory research to early commercialization attempts [13,14], there is the need for a physics-based model that can accurately describe and simulate the behavior of this novel system in practically relevant configurations. Such a model would provide a deeper understanding of the electrochemical processes involving the variation of the salt concentration in the electrolyte and assist in the proper design of dual-ion batteries. So
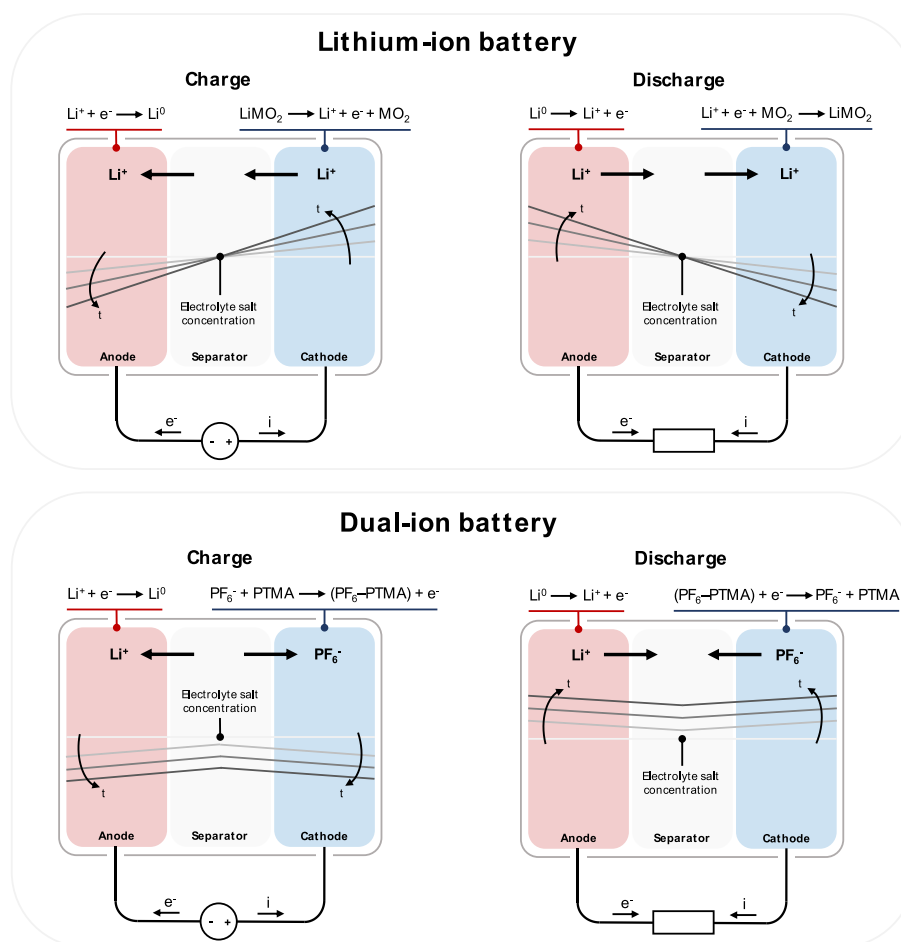
Fig. 1. Schematic depiction of the charge and discharge processes of a lithium-ion battery (top) and a dual-ion battery (bottom), with the expected trend of the electrolyte salt concentration.

far, dual-ion batteries have been the focus of only mechanistic computational studies, involving Density Functional Theory (DFT) and Molecular Dynamics (MD), which investigated the interaction between anions and host structures in terms of electrochemical stability, potential of the electrochemical reaction, or reversibility of the insertion process [15–18]. However, the size and timescale of these models does not allow the simulation of entire batteries for full charge and discharge cycles or other types of characterization tests such as electrochemical impedance spectroscopy (EIS). A class of models that is suited for this objective are macroscale physic-based models, based on partial differential equations that aim to reproduce the physical processes involved in the battery operation. As far as the authors know, only one work in literature employed such a model in a system that included an anion-adsorbing cathode material, which was however mixed with a lithium-ion cathode material, and no experimental data were presented to validate the results of the simulations [19].

In this paper, a modified version of the standard pseudo-2D Doyle-Fuller-Newman (DFN) model, a widely used macroscale physical model originally developed for lithium-ion batteries [12], is proposed to account for the different redox reactions that occur at the cathode and anode of dual-ion batteries. The model can simulate the variation of salt concentration in the electrolyte during charge and discharge of the dual-ion battery, including the concentration gradients that form along the battery thickness. It has been validated against cycling and impedance experimental data from dual-ion batteries with a mixture of poly(2,2,6,6-tetramethyl-1-piperidinyloxy methacrylate) (PTMA), belonging to the anion-interacting p-type class of organic materials, and multi-walled carbon nanotubes as cathode electrode material, a thick glass fiber separator, a lithium metal anode, and 1 M LiPF$_6$ in EC:DMC 1:1 as the electrolyte in a lab-scale three-electrode cell setup. This work shows how the model can serve as a valuable tool for supporting the design of dual-ion batteries, which entails a delicate balance between separator thickness, salt concentration, porosity and amount of cathode active material.

2. Materials and methods

2.1. Synthesis of the PTMA/MWCNT mixture

The synthesis of the poly(2,2,6,6-tetramethyl-1-piperidinyloxy methacrylate) (PTMA)/multi-walled carbon nanotubes (MWCNT) mixture was carried out according to the bulk radical polymerization procedure described in Vlad et al. [20] 17 g of 2,2,6,6-tetramethyl-4-piperidyl methacrylate (TMPM 98%, *TCI*) and 115.11 mg of azobisisobutyronitrile (AIBN, recrystallized in ethanol, *TCI*) were dissolved in acetone (*VWR*, technical grade) and 520 μl of ethylene glycol dimethacrylate as crosslinking agent (EGDME 98%, *Acros Organics*) were subsequently added. The solvent was evaporated in a rotary evaporator first and then in a Schlenk line connected to a vacuum pump with a nitrogen trap.

The dried precursor mixture was inserted in a ball mill apparatus (Type S1, *Retsch GmbH*) with three agate balls of 3 cm of diameter, and 3 g of MWCNTs (industrial grade, *Nanocyl*) were added. The precursor mixture was ball-milled for 1 h at 80% of the maximum speed, and it was then put in a 500 ml cylindrical glass reactor, which was purged with argon gas three times, and then left in a stirred oil bath at 80 °C overnight for the polymerization reaction.

The product (poly(2,2,6,6-tetramethyl-1-piperidyl methacrylate) (PTMPT) with 15% wt. MWCNT) was removed from the reactor after cooling down to room temperature by swelling it with dichloromethane (DCM, technical grade, *VWR*) and then washed with the same solvent. After drying with rotary evaporator and vacuum pump, the polymer-carbon mixture was ball-milled for 1 h at 80% of the maximum speed of the ball mill apparatus.

The oxidation of PTMPT was performed by taking 20 g of the polymer-carbon mixture and dispersing it in methanol (technical grade,

VWR) in a 1L round bottom glass reactor by stirring with a magnetic bar, and then adding 4.64 g of sodium tungstate (Na$_2$WO$_4$ 99%, *Sigma Aldrich*), 3 g of ethylenediaminetetraacetic sodium salt (EDTA 98.5%, *Sigma Aldrich*), and 34 ml of 30% aqueous solution of hydrogen peroxide (H$_2$O$_2$, *Sigma Aldrich*). The mixture was left reacting for 48 h in a stirred oil bath at 60 °C with an air-cooled reflux condenser. The reacted mixture was then vacuum filtered several times with water/methanol 1:1 vol:vol mixture until the washing solution remained colorless, dried in a vacuum oven (*Binder*) at 60 °C overnight, and then ball-milled for 1 h at 80% of the maximum speed of the ball mill apparatus.

The final product (PTMA with 15% wt. MWCNT) consisted in a fine black powder, and the overall mass yield was ≈85% with respect to the sum of the mass of TMPM and MWCNTs used as precursors. This active material has a theoretical specific capacity of 111 mAh·g^{-1}.

2.2. Electrode preparation

The PTMA-based cathodes for the electrochemical characterization tests were prepared with a water-based procedure. 900 mg of the PTMA/MWCNT mixture, 50 mg of conductive carbon (Super C45, *IMERYS*), 30 mg of carboxymethyl cellulose from a 3% wt. aqueous solution (CMC, *Walocel* CRT 2000 PPA 12), 20 mg of styrene-butadiene rubber from a 40% latex solution (SBR, *Zeon* BM451-B), and 500 mg of deionized water were mixed in a planetary centrifugal mixer (ARE-250, *THINKY*) at 2000 rpm for 10 min. The weight ratio between the electrode components is 90:5:3:2 (PTMA/MWCNT:C45:CMC:SBR). The mixture was coated on a carbon-coated aluminum foil (*Wellcos*) with a wet thickness of 120 μm, and the slurry-coated foil was dried overnight in a dry room (dew point < −70 °C). 18 mm Ø electrodes were cut from the coated foil, pressed with 1 ton-force, and dried at 80 °C for 12 h in a Büchi oven connected to a vacuum pump (<1·10^{-3} mbar) before being transferred into an argon-filled glove box (MB200B ECO, *MBraun*, O$_2$ < 0.1 ppm, H$_2$O < 0.1 ppm). The obtained dry thicknesses were in the 55-65 μm range, and the active material mass loadings between 3.7 and 3.9 mg cm^{-2}. The scanning electron microscopy (SEM) images of the PTMA/MWCNT powder and electrodes were taken with a ZEISS Crossbeam XB340 at a working voltage of 5 kV.

2.3. Electrochemical characterization

The galvanostatic charge/discharge tests and electrochemical impedance spectroscopy tests were performed with a three-electrode ECC-PAT-Core cell (*EL-CELL GmbH*), using a 18 mm Ø PTMA-based electrode as cathode, a 21 mm Ø glass fiber Whatman GF/A separator soaked in 200 μl of the electrolyte solution (1 M LiPF$_6$ in ethyl carbonate (EC)/dimethyl carbonate (DMC), 1:1 w/w), a 18 mm Ø lithium metal disk (500 μm, battery grade, *Honjo*) as anode, and a lithium-coated nickel ring (*EL-CELL GmbH*) as reference electrode, inserted between the cathode and the separator.

All the electrochemical measurements were carried out at 20 °C. Both the galvanostatic charge/discharge tests and EIS tests were performed with a Biologic VMP battery cycler equipped with a frequency response analyzer. The EIS was performed with the potentiostatic mode, in the 100 kHz–100 mHz frequency range, with 10 points for every decade, and a voltage amplitude of 10 mV. The cells performed 3 cycles at 0.1, then 3 cycles at 0.2C, 0.5C, 1C, 2C, and 5C, followed by 20 cycles at 1C. This whole procedure was repeated two times, with the impedance measurements made each time before the 0.2C cycles, measuring 10 impedance spectra at different state of charge (SOC) points along the 0.1C discharge that preceded the 0.2C cycles.

2.4. Model characteristics

The macroscale physical model was implemented in the software COMSOL Multiphysics®, version 6.0, using the Battery Design Module. The direct, fully coupled solver uses the nonlinear Newton's method,

with the implicit backward differentiation formula for the time stepping. The EIS is simulated with COMSOL Multiphysics® by linearizing the model around the chosen open-circuit potential and performing the Laplace transform [21].

3. Results and discussion

3.1. Physical model

In this section, the developed physical model for dual-ion batteries is reported with the objective to show the key differences with the classic DFN model for lithium-ion batteries.

The 1D domain of the model is represented in Fig. 2, composed by a dimensionless point representing the lithium metal anode for the cation redox reaction ($x = 0$), a porous separator (from $x = 0$ to $x = L_{sep}$), and a porous cathode for the anion redox reaction (from $x = L_{sep}$ to $x = L_{sep} + L_{pos}$). In each node of the cathode domain, analogously with the standard DFN model, a particle with radius r is present, to simulate the distribution of the anion concentration in the cathode material.

The model's equations are presented in Table 1, together with the boundary conditions of the partial differential equations (PDEs), while the step-by-step derivation of the model can be found in the Supporting Information. The meaning of all the used symbols is in Table 3. Being a 1D model, the gradients written in the following equations have to be intended as the derivative along the x-axis (or the r-axis, for the conservation of mass in the solid electrode).

In the separator domain we have $\bar{j} = 0$, since there is no electrochemical reaction, while the lithium metal anode is modelled as an electrode surface, which becomes a dimensionless point in the 1D model, and a flux of ions is used as boundary condition for the conservation of mass in the liquid electrode in $x = 0$ (eq. 8). The potential $\overline{\varphi_s}$ is set to 0 V in correspondence of the anode, and the lithium metal overpotential is calculated from the Butler-Volmer equation related to lithium-ion batteries. For the lithium metal anode, $E_{ocp} = 0$, while for the cathode the open circuit potential is taken from experimental data, function of the concentration of anions in the material, and inserted in the model as lookup table (Fig. S1). The exchange current density i_0 in the Butler-Volmer equation is assumed to be a constant both for the cathode and for the anode side. The properties of the electrolyte are modelled according to the empirical equations given in Landesfeind & Gasteiger [22], where the ionic conductivity, the salt diffusion

coefficient, the activity coefficient and the transference number of LiPF$_6$ in EC:DMC 1:1 are measured in a wide range of salt concentrations and temperatures (see eq. S69–S72 in the Supporting Information). Compared to the formal derivation reported in the Supporting Information, which focuses on the basic model, the contribution of the double layer capacitance in the charge conservation equations in the electrode (eq. 1) and the electrolyte (eq. 3) is considered, too [23].

The current applied to the battery is calculated according to the capacity Q and the desired C-rate. The initial state of charge (SOC) is inserted as a parameter and the initial concentration of anions in the cathode particles and the initial salt concentration in the electrolyte are calculated respectively with eq. 14 and 15. The galvanostatic cycling is simulated in the 3-4 V range, while the EIS is modelled at different SOCs in open circuit voltage conditions, as in the respective experiments. A contact resistance R_{ext} is added to the model to take into account the eventual impact of the cables resistance in the experimental results.

The main differences between the DFN model for dual-ion batteries and lithium-ion batteries are summarized in the following points:

- The redox reaction at the dual-ion battery cathode involves the consumption of anions during charge and their generation during discharge. The current density i is by convention positive when the battery is charged, i.e., when the electrons flow from the cathode to the anode, while j is by convention positive when exiting the cathode material. During charge the flux of anions j is negative, as we observe a consumption of ions with the flow from electrolyte to electrode. During discharge, j becomes positive, as the anions are released by the electrode and migrate in the electrolyte, but i is then negative due to the switch of the current direction. Hence, i and j always have opposite signs in a dual-ion battery, while for the same line of reasoning, in a lithium-ion battery they have the same sign (eq. 10) (see Fig. 1 for the depiction of the ion and current fluxes in the two types of battery).
- This affects the formulation of the conservation of charge in the solid electrode and the liquid electrolyte, where the sign of the right-hand terms of the two equations is the opposite of the corresponding ones of a lithium-ion battery model (see eq. S39 and S56).
- The mass conservation in the liquid electrolyte is affected too. In this case, the transference number multiplied by the ion flux in the right-hand side of eq. 7 is t_+^0, the one associated to the cations. Instead, in the standard DFN model for lithium-ion batteries, this term is
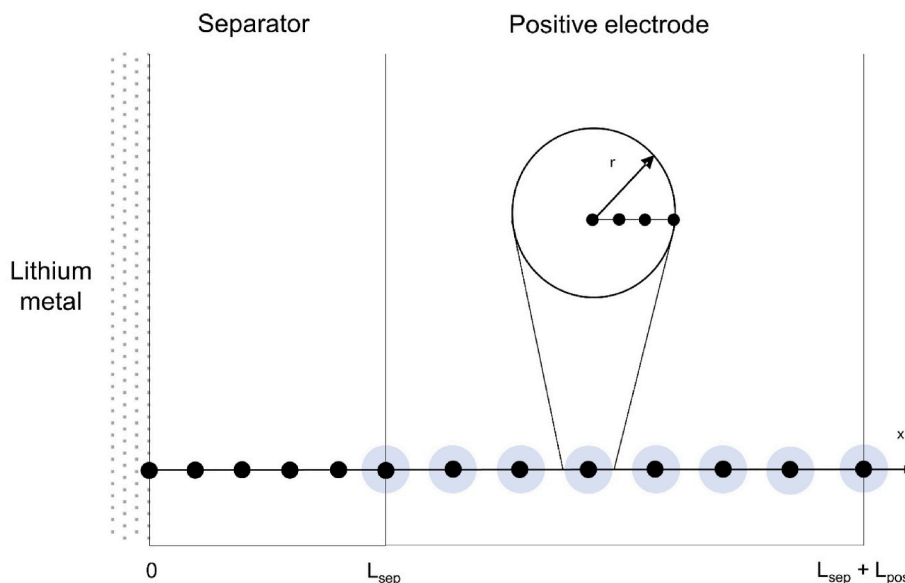
Fig. 2. Representation of the model domain.

Table 1
Equations and boundary conditions of the dual-ion battery model.

Conservation of charge in the solid electrode

$$\nabla \bullet (-\sigma_{eff}\nabla\overline{\varphi_s}) = a_s\bar{j}F + a_sC_{dl}\nabla(\overline{\varphi_s} - \overline{\varphi_e}) \tag{1}$$

$$\begin{cases} \nabla\overline{\varphi_s}\big|_{x=L_{sep}+L_{pos}} = -\dfrac{i}{\sigma_{eff}} \ \ \nabla\overline{\varphi_s}\big|_{x=L_{sep}} = 0 \ \ \overline{\varphi_s}\big|_{x=0} = 0 \end{cases} \tag{2}$$

Conservation of charge in the liquid electrolyte

$$\nabla \bullet \left(-\kappa_{eff}\nabla\overline{\varphi_e} - \dfrac{2\kappa_{eff}RT}{F}(t_+^0 - 1)\left(1 + \dfrac{\partial f_\pm}{\partial\ln c_e}\right)\nabla\ln\overline{c_e}\right) = -a_s\bar{j}F - a_sC_{dl}\nabla(\overline{\varphi_s} - \overline{\varphi_e}) \tag{3}$$

$$\begin{cases} -\kappa_{eff}\nabla\overline{\varphi_e} - \dfrac{2\kappa_{eff}RT}{F}(t_+^0 - 1)\left(1 + \dfrac{\partial f_\pm}{\partial\ln c_e}\right)\nabla\ln\overline{c_e}\Big|_{x=L_{sep}+L_{pos}} = 0 \ \ -\kappa_{eff}\nabla\overline{\varphi_e} - \dfrac{2\kappa_{eff}RT}{F}(t_+^0 - 1)\left(1 + \dfrac{\partial f_\pm}{\partial\ln c_e}\right)\nabla\ln\overline{c_e}\Big|_{x=0} = i \end{cases} \tag{4}$$

Conservation of mass in the solid electrode

$$\dfrac{\partial c_s}{\partial t} = \dfrac{1}{r^2}\dfrac{\partial}{\partial r}\left(D_s r^2\dfrac{\partial c_s}{\partial r}\right) \tag{5}$$

$$\begin{cases} \nabla c_s\big|_{r=0} = 0 \\ \nabla c_s\big|_{r=R_p} = -\bar{j} \end{cases} \tag{6}$$

Conservation of mass in the liquid electrolyte

$$\varepsilon_e\dfrac{\partial\overline{c_e}}{\partial t} = \nabla\cdot(D_{e,eff}\nabla\overline{c_e}) + a_s t_+^0\bar{j} \tag{7}$$

$$\begin{cases} \nabla\overline{c_e}\big|_{x=L_{sep}+L_{pos}} = 0 \ \ D_{e,eff}\nabla\overline{c_e}\big|_{x=0} = (1 - t_+^0)\bar{j} \end{cases} \tag{8}$$

Electrochemical reaction (Butler-Volmer equation)

$$i = i_0\left(\exp\left\{\dfrac{(1-\alpha)nF\eta}{RT}\right\} - \exp\left\{-\dfrac{\alpha nF\eta}{RT}\right\}\right) \tag{9}$$

$$\begin{cases} i\big|_{x=0} = \bar{j}F \\ i\big|_{x=L_{sep}+L_{pos}} = -\bar{j}F \end{cases} \tag{10}$$

Other definitions

$$V = \overline{\varphi_s}\big|_{x=L_{sep}+L_{pos}} - \overline{\varphi_s}\big|_{x=0} + R_{ext}\,i \tag{11}$$

$$\eta = \overline{\varphi_s} - \overline{\varphi_e} - E_{ocp} \tag{12}$$

$$Q = A\,\varepsilon_{s,pos}\,L_{pos}\,c_{max,pos}\,F\,(SOC_{max,pos} - SOC_{min,pos}) \tag{13}$$

$$c_{s,0,pos} = c_{s,max,pos}\,[SOC(SOC_{max,pos} - SOC_{min,pos}) + SOC_{min,pos}] \tag{14}$$

$$c_{e,0} = c_{e,ref}\left(1 - \dfrac{SOC\,\dfrac{Q}{F}}{c_{l,ref}A\,(\varepsilon_{e,sep}L_{sep} + \varepsilon_{e,pos}L_{pos})}\right) \tag{15}$$

---

multiplied by t_-^0, the anion transference number (see eq. S47). This arises from the fact that $a_s\bar{j}$ anions are generated in the volume during the electrochemical reaction and $a_s t_-^0\bar{j}$ are transported out of the volume due the electrical current. Since the sum of the anion and cation transference numbers is equal to 1, the number of anions that stays in the volume is $a_s t_+^0\bar{j}$. The same line of reasoning applies for the lithium-ion battery case, with inverted transference numbers.

- Finally, the initial electrolyte salt concentration $c_{e,0}$ becomes a function of the SOC of the cell in a dual-ion battery. In fact, according to the SOC, a fraction of the anions present in the electrolyte will be stored in the cathode as a consequence of the electrochemical reaction, and the salt present in the electrolyte has to be consumed to provide anions for such a reaction. The higher the SOC, the higher the amount of anions in the cathode, and hence the lower $c_{e,0}$. The fraction of eq. 15 represents the ratio between the moles of anions present in the cathode and the maximum amount of moles of anions available in the electrolyte. In the lithium-ion battery model, $c_{e,0}$ is a constant, since its average value does not change during the operation of the battery.

3.2. Comparison between model results and experimental data

In Table 2, the value of the parameters used for the simulation of the dual-ion battery is reported. The proposed parameter set has been derived by measuring, estimating, and assuming the numerical values, and it can be refined with further measurements on the studied system in future works. However, the aim is not finding the definitive parameter set that can describe univocally the system, but to show that the capability of the model to reproduce galvanostatic charge/discharge and EIS experimental results obtained with a laboratory-scale PTMA/Li metal battery.

The variation of the electrolyte salt concentration during the operation of the dual-ion battery is shown in Fig. 3c and Fig. 3d, obtained by simulating a 10C charge and discharge cycle in galvanostatic mode in the model (Fig. 3a). Upon charge (Fig. 3c), the average concentration of the salt decreases, since the electrochemical reactions at the anode and the cathode that are both consuming the electrolyte ions, while during the subsequent discharge (Fig. 3d) the ions are released by the electrodes and the initial average salt concentration is restored. The gradient of concentration along the thickness of the cell is due to mass transport limitations in the electrolyte due to the high employed current (10C).

In lithium-ion battery simulations with an analogous model, the salt concentration usually develops a gradient along the thickness of the

Table 2
Value of the model parameters for the simulation of a PTMA|Li metal cell.

Parameter	Unit of measurement	Anode	Separator/ Electrolyte/ Cell	Cathode	Reference
α	$[-]$	0.5	–	0.5	Assumed
a_s	$[m^{-1}]$	–	–	$1 \bullet 10^5$	Assumed
A	$[m^2]$	–	$2.545 \bullet 10^{-4}$	–	Measured
bg	$[-]$	–	1.5	1.5	Assumed
$c_{e,ref}$	$[mol \bullet m^{-3}]$	–	1000	–	Measured
$c_{s,max}$	$[mol \cdot m^{-3}]$	–	–	4375	Estimated
C_{dl}	$[F \bullet m^{-2}]$	–	–	0.01	Assumed
D_s	$[m^2 \bullet s^{-1}]$	–	–	$2.5 \bullet 10^{-13}$	Assumed
ε_e	$[-]$	–	0.9	0.374	Estimated
ε_s	$[-]$	–	–	0.505	Estimated
i_0	$[A \bullet m^{-2}]$	5	–	2.7	Assumed
L	$[m]$	–	$260 \bullet 10^{-6}$	$62.6 \bullet 10^{-6}$	Measured
R_{ext}	$[\Omega \bullet m^2]$	–	$2.5 \bullet 10^{-4}$	–	Estimated
R_p	$[m]$	–	–	$10 \bullet 10^{-6}$	Assumed
σ	$[S \bullet m^{-1}]$	–	–	$2.0 \bullet 10^{-2}$	Assumed
SOC_{min}	$[\%]$	–	–	0	Assumed
SOC_{max}	$[\%]$	–	–	100	Assumed
T_0	$[K]$	293.15	293.15	293.15	Measured

battery, especially when high currents are used, but the average value remains always constant, since the same number of lithium ions is consumed in one electrode and generated in the other [12]. In case of poorly conductive electrolytes and/or large C-rates applied for long time, the salt concentration can locally approach zero in lithium-ion batteries, but as soon as the load is disconnected, the diffusion processes starts to equilibrate the salt concentration and to restore its initial value. Instead, the electrolyte salt can potentially get completely depleted in the dual-ion case: in the results of Fig. 3c, at the end of the discharge the average salt concentration value is ≈ 450 mol m^{-3}. With a thicker cathode, where more active material has to be charged, or with a thinner or less porous separator, where less electrolyte and hence less salt is available, the salt concentration can reach zero before the charge process is fully complete, curtailing the energy that is possible to store in the dual-ion battery. This interplay between the size and porosity of the

electrodes and separator and salt concentration in the electrolyte is then crucial to the design of this class of batteries.

Two experimental discharge curves at 0.2C and 5C are compared with model results at the same C-rates in Fig. 3b. The data were obtained by measuring the PTMA cathode potential against a pseudo-reference lithium metal electrode in a three-electrode configuration, to eliminate the influence of the lithium metal counter electrode. Therefore, in the simulations the cathode voltage (and the cathode impedance spectra shown in the next paragraphs) are measured against a modelled reference electrode placed in the separator next to the cathode. The model is able to well reproduce the experimental voltage-specific capacity relationship both at low and high current, with only some discrepancy in the voltage at low state of charge in the latter case, probably due to the solid diffusion modelling.

The only other work which proposed a macroscale physical modelling of a PTMA-based electrode did not consider the influence of diffusion of anions in the active material, since they assumed that the PTMA was forming a gel with the electrolyte and that no solid diffusion was taking place [19]. In our simulations, it was necessary to include the spherical particle modelling of the anion particles to reproduce the variation of specific capacity experimentally measured at different current rates. The anion diffusion coefficient in the solid D_s was set to a value of $2.5 \cdot 10^{-13}$ m^2 s^{-1}, a relatively high value when compared to typical lithium diffusion coefficients in inorganic cathode materials [24]. Nevertheless, the influence of the solid diffusion on the results of the simulations is determined by the radius of the particles, too. Herein, it was assumed to be 10 μm, but SEM images of both the PTMA powder (Fig. S2a) and the PTMA electrodes (Fig. S2b) did not show a clear particle size or shape, rather indicating an amorphous morphology. Hence, this parameter could be subject of refinement in future works, possibly considering the modelling of a particle size distribution instead of a single particle size as in this model [25].

The comparison between the impedance spectrum between 100 kHz and 100 mHz at 53.4% SOC obtained in the model and the experimental one at the same SOC can be found in Fig. 4a. The two spectra agree very well in the high-mid frequency range, where the charge transfer resistance of the electrochemical reaction is usually identified. The short low
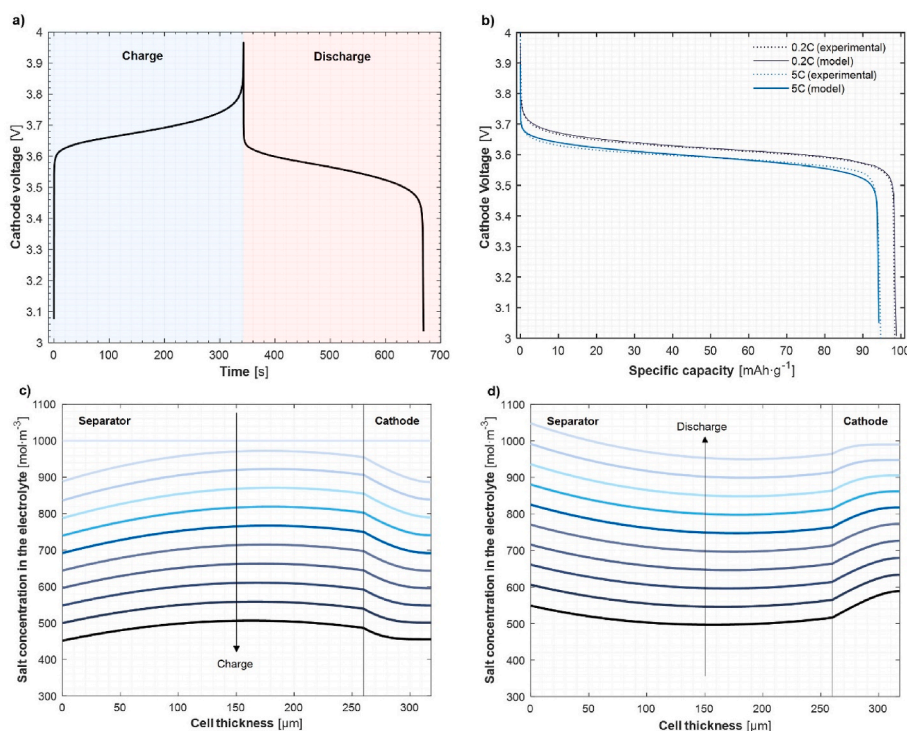
Fig. 3. a) Voltage vs. time during a simulated galvanostatic charge and discharge cycle at 10C of the PTMA/Li metal cell, b) Comparison between the voltage vs. specific capacity characteristics of the model results (solid line) and the experimental data (dotted line) at 0.2C and 5C, c) Selected electrolyte salt concentration profiles at different time steps during the simulated 10C charge of the of the PTMA/ Li metal cell of Fig. 3a, d) Selected electrolyte salt concentration profiles at different time steps during the simulated 10C discharge of the of the PTMA/Li metal cell of Fig. 3a.

frequency impedance tail, associated to diffusion phenomena, is well reproduced, too. The main discrepancy between the two spectra is the second, small semicircle between 4.5 and 5 Ω in the real axis, which could be associated to an additional interfacial phenomenon (such as cathode electrolyte interphase), a wide particle size distribution, or an incomplete wetting of the electrode, phenomena which are not considered in the current state of the model's equations [21]. Hence, with the current state of the model, no combination of parameters could reproduce this two-semicircle spectrum that is experimentally measured.

By comparing the simulated and the experimental spectra in the whole SOC range in Fig. 4b, the trend of the model results is seen to follow the one of the EIS data, with a decrease of the low frequency diffusion resistance when going towards the mid SOC region, a sharp increase of the same resistance at very low and very high SOCs, and a fairly constant value of the semicircle(s) in the high and medium frequency range. The lower slope of the model low frequency impedance at 99.8% and 0.3% SOC compared to the corresponding ones in the experimental data suggests that the for the model a semi-infinite diffusion approximation is still valid in the chosen frequency range, while the shape of the experimental data resembles the one of a limited diffusion case [26]. Hence, as suggested above in the discussion of the galvanostatic cycling data, an improvement of the modelling of the solid diffusion in the electrode particles may be necessary to well reproduce also this frequency range at extreme SOCs.

3.3. Application of the model for the design of dual-ion batteries

Despite the discussed limitations, the experimental data agrees with the model results, and the simulated trend of the electrolyte salt concentration during battery charge and discharge follows the one expected from theory. These findings indicate that the model can successfully simulate the dual-ion battery operation.

Other than obtaining a deeper mechanistic understanding of the studied system, this model can well support the design of dual-ion batteries that respect the constraints imposed by the anion-involving redox reaction at the cathode, while optimizing key design parameters such as separator porosity and thickness, cathode porosity and thickness, and electrolyte salt concentration.

To give an example which uses the starting electrolyte salt concentration as design parameter, the dual-ion battery is simulated with the values reported in Table 1, except for a decrease of the separator thickness and porosity ($L_{sep} = 75\,\mu m$, $\varepsilon_{e,sep} = 0.5$). The resulting lower

separator volume can accommodate only about one sixth of the electrolyte that is contained in the separator geometry of Table 1. Hence, the availability of anions for the electrochemical reaction decreases, and in fact the maximum specific capacity reached by the dual-ion battery during charge with this configuration is about 42 mAh·g^{-1}, with the salt electrolyte concentration that approaches zero at the cathode-current collector interface (Fig. 5a). By increasing the starting salt concentration in the electrolyte to 2000 mol m^{-3} (2 M), the reached specific capacity in charge doubles, reaching 86 mAh·g^{-1}, but only with a 3000 mol m^{-3} (3 M) starting concentration the full specific capacity is restored, and the salt concentration is still 970 mol m^{-3} at the end of the charge. From Fig. 5b it can be seen how the average electrolyte ionic conductivity in the battery varies sensibly along the three cases. For the 1 M electrolyte, the conductivity decreases almost monotonically, while with the 2 M and 3 M electrolyte an increase is also observed, due to the lower conductivity of the solution at high concentrations [22,27]. This has an impact on the voltage profile during charge, and it is especially evident in the 3 M case, where the overpotential at low SOC is larger than in the other two simulated curves.

4. Conclusions

In conclusion, this paper proposes a modified version of the Doyle-Fuller-Newman model to simulate the operation of dual-ion batteries, which involve both cations and anions in the redox reactions respectively at the anode and the cathode. The developed model successfully accounts for the variation of the average salt concentration in the electrolyte during the charge and discharge of the battery. The model is validated against experimental data from dual-ion batteries with PTMA as cathode, demonstrating its ability to well simulate the operation of these batteries.

This model has important implications for the design of dual-ion batteries, which require careful consideration of the electrolyte's salt concentration due to the involvement of anions in the redox reaction. By using the developed model, it is possible to optimize key design parameters such as separator porosity and thickness, cathode porosity and thickness, and electrolyte salt concentration to improve the performance of dual-ion batteries and obtain practical solutions.

This article, having introduced a macroscopic physical modelling of a dual-ion battery, can also serve as a starting point for a more accurate mechanistic description of this peculiar class of batteries, with the objective of overcoming the discussed limitations. The proposed model
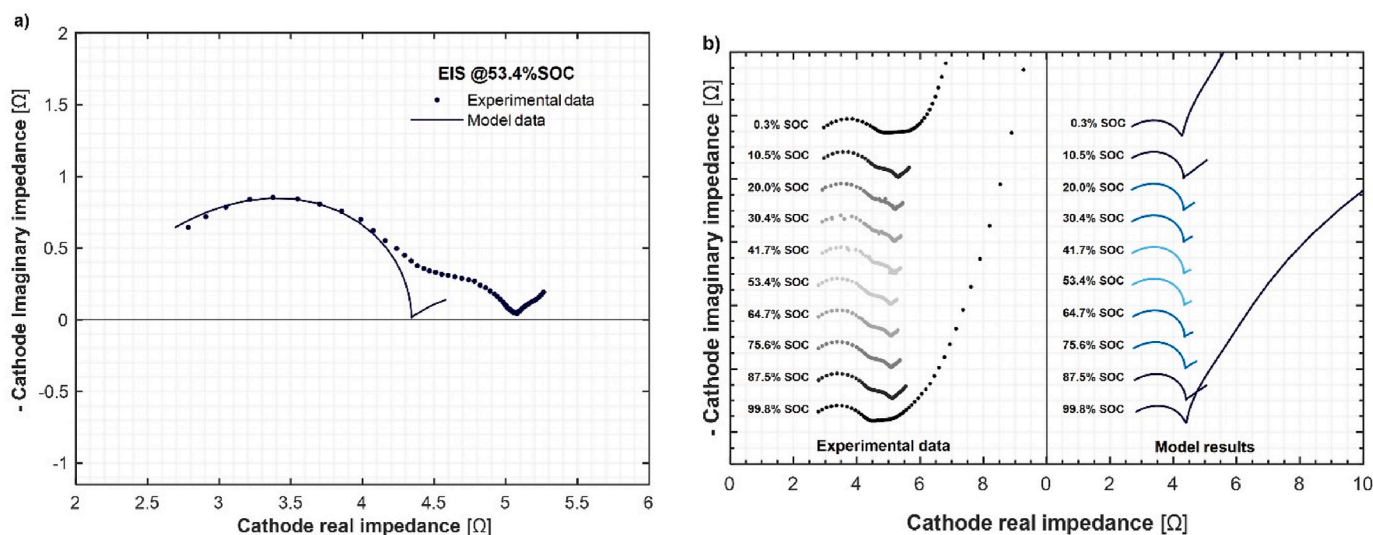
Fig. 4. a) Comparison between the experimental (dotted) and the modelled (solid) impedance spectrum at 53.4% SOC, b) Comparison between the experimental (grey scale, dotted) and the modelled (blue scale, solid line) impedance spectra at all the measured SOCs. (For interpretation of the references to color in this figure legend, the reader is referred to the Web version of this article.)
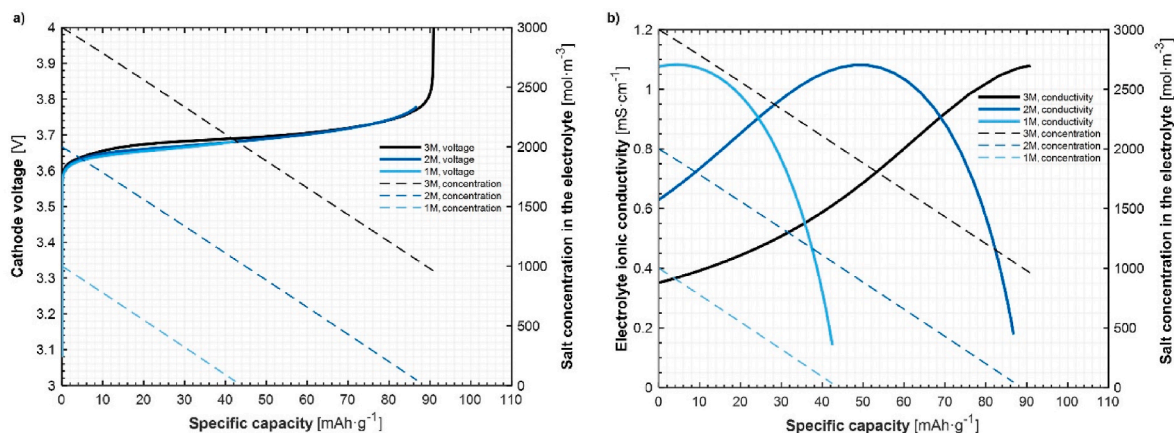
Fig. 5. a) Voltage, b) average ionic conductivity, and average salt concentration in the electrolyte vs. specific capacity for the simulated PTMA/Li metal cells with three different starting salt molar concentrations in the electrolyte during a 10C charge.

can also be readily adapted to other anion-hosting materials, such as graphite or other p-type organic electrode materials.

CRediT authorship contribution statement

Alessandro Innocenti: Conceptualization, Methodology, Investigation, Software, Visualization, Formal analysis, Writing – original draft. **Isaac Álvarez Moisés:** Resources, Investigation, Writing – review & editing. **Jean-François Gohy:** Resources, Writing – review & editing, Supervision, Funding acquisition. **Stefano Passerini:** Conceptualization, Writing – review & editing, Supervision, Funding acquisition.

Declaration of competing interest

The authors declare that they have no known competing financial interests or personal relationships that could have appeared to influence the work reported in this paper.

Data availability

Data will be made available on request.

Appendix A. Supplementary data

Supplementary data to this article can be found online at https://doi.org/10.1016/j.jpowsour.2023.233429 and at the Zenodo repository https://doi.org/10.5281/zenodo.8131099.

Appendix

Table 3
Table of symbols used in the model definition

Symbol	Unit of measurement	Description	Symbol	Unit of measurement	Description
Latin			**Greek**		
a	$[m^{-1}]$	Specific active area	α	$[-]$	Transfer coefficient
A	$[m^2]$	Electrode area	ε	$[-]$	Volume fraction
c	$[mol \cdot m^{-3}]$	Lithium concentration	η	$[V]$	Overpotential
C_{dl}	$[F \cdot m^{-2}]$	Double layer capacitance	κ	$[S \cdot m^{-1}]$	Ionic conductivity
D	$[m^2 \cdot s]$	Diffusion coefficient	φ	$[V]$	Electric potential
E_{ocp}	$[V]$	Open circuit potential	σ	$[S \cdot m^{-1}]$	Electronic conductivity
F	$[A \cdot s \cdot mol^{-1}]$	Faraday constant	**Subscript**		
$\left(1 + \frac{\partial f_{\pm}}{\partial \ln c_e}\right)$	$[-]$	Activity coefficient	**0**		initial
i	$[A \cdot m^{-2}]$	Current density	e		electrolyte
i_0	$[A \cdot m^{-2}]$	Exchange current density	eff		effective
j	$[mol \cdot m^{-2} \cdot s^{-1}]$	Lithium molar flux	max		maximum
L	$[m]$	Cell component length	min		minimum
Q	$[mAh]$	Capacity	pos		positive
R	$[J \cdot mol^{-1} \cdot K^{-1}]$	Universal gas constant	ref		reference
R_{ext}	$[\Omega \cdot m^2]$	External resistance	s		solid
R_p	$[m]$	Particle radius	sep		separator
SOC	$[-]$	State of charge	**Superscript**		
t_0^+	$[-]$	Cation transference number	bg		Bruggeman coefficient

Table 3 (*continued*)

Symbol	Unit of measurement	Description	Symbol	Unit of measurement	Description
T	[K]	Temperature	**Coordinate**		
V	[V]	Cell voltage	x		Linear coordinate
			r		Radial coordinate
			t		Time

References

[1] B. Dunn, H. Kamath, J.-M. Tarascon, Electrical energy storage for the grid: a battery of choices, Science 334 (2011) 928–935, https://doi.org/10.1126/science.1212741.

[2] R. Schmuch, R. Wagner, G. Hörpel, T. Placke, M. Winter, Performance and cost of materials for lithium-based rechargeable automotive batteries, Nat. Energy 3 (2018) 267–278, https://doi.org/10.1038/s41560-018-0107-2.

[3] Y. Tian, G. Zeng, A. Rutt, T. Shi, H. Kim, J. Wang, et al., Promises and challenges of next-generation "beyond Li-ion" batteries for electric vehicles and grid decarbonization, Chem. Rev. 121 (2021) 1623–1669, https://doi.org/10.1021/acs.chemrev.0c00767.

[4] F. Duffner, N. Kronemeyer, J. Tübke, J. Leker, M. Winter, R. Schmuch, Post-lithium-ion battery cell production and its compatibility with lithium-ion cell production infrastructure, Nat. Energy 6 (2021) 123–134, https://doi.org/10.1038/s41560-020-00748-8.

[5] L. Zhang, H. Wang, X. Zhang, Y. Tang, A review of emerging dual-ion batteries: fundamentals and recent advances, Adv. Funct. Mater. 31 (2021), 2010958, https://doi.org/10.1002/adfm.202010958.

[6] M. Liu, W. Zhang, W. Zheng, Spreading the landscape of dual ion batteries: from electrode to electrolyte, ChemSusChem 16 (2023), e202201375, https://doi.org/10.1002/cssc.202201375.

[7] H. Jiang, Z. Chen, Y. Yang, C. Fan, J. Zhao, G. Cui, Rational design of functional electrolytes towards commercial dual-ion batteries, ChemSusChem 16 (2023), e202201561, https://doi.org/10.1002/cssc.202201561.

[8] M. Tebyetekerwa, T.T. Duignan, Z. Xu, X. Song Zhao, Rechargeable dual-carbon batteries: a sustainable battery technology, Adv. Energy Mater. 12 (2022), 2202450, https://doi.org/10.1002/aenm.202202450.

[9] M. Cugnet, S. Laruelle, S. Grugeon, B. Sahut, J. Sabatier, J.-M. Tarascon, et al., A mathematical model for the simulation of new and aged automotive lead-acid batteries, J. Electrochem. Soc. 156 (2009) A974, https://doi.org/10.1149/1.3224868.

[10] J.R. Dahn, J.A. Seel, Energy and capacity projections for practical dual-graphite cells, J. Electrochem. Soc. 147 (2000) 899, https://doi.org/10.1149/1.1393289.

[11] T. Placke, A. Heckmann, R. Schmuch, P. Meister, K. Beltrop, M. Winter, Perspective on performance, cost, and technical challenges for practical dual-ion batteries, Joule 2 (2018) 2528–2550, https://doi.org/10.1016/j.joule.2018.09.003.

[12] T.F. Fuller, M. Doyle, J. Newman, Simulation and optimization of the dual lithium ion insertion cell, J. Electrochem. Soc. 141 (1994) 1–10, https://doi.org/10.1149/1.2054684.

[13] A. Wild, M. Korell, S. Münch, A. Lex-Balducci, J. Brendel, U.S. Schubert, Solid electrolyte for organic batteries US Patent 2023. Available: https://patents.google.com/patent/US11637318B2/en.

[14] S. Muench, R. Burges, A. Lex-Balducci, J.C. Brendel, M. Jäger, C. Friebe, et al., Adaptation of electrodes and printable gel polymer electrolytes for optimized fully organic batteries, J. Polym. Sci. 59 (2021) 494–501, https://doi.org/10.1002/pol.20200746.

[15] K. Tasaki, Density functional theory study on structural and energetic characteristics of graphite intercalation compounds, J Phys Chem C Nanomater Interfaces 118 (2014) 1443–1450, https://doi.org/10.1021/jp409700q.

[16] K. Beltrop, P. Meister, S. Klein, A. Heckmann, M. Grünebaum, H.-D. Wiemhöfer, et al., Does size really matter? New insights into the intercalation behavior of anions into a graphite-based positive electrode for dual-ion batteries, Electrochim. Acta 209 (2016) 44–55, https://doi.org/10.1016/j.electacta.2016.05.012.

[17] J. Vatamanu, O. Borodin, M. Olguin, G. Yushin, D. Bedrov, Charge storage at the nanoscale: understanding the trends from the molecular scale perspective, J Mater Chem A Mater Energy Sustain 5 (2017) 21049–21076, https://doi.org/10.1039/c7ta05153k.

[18] K. Beltrop, J.C. Madrid Madrid, P. Meister, A. Heckmann, M. Winter, T. Akbay, et al., Experimental and computational studies of electrochemical anion intercalation into graphite from target-oriented designed borate-based ionic liquid electrolytes, J. Power Sources 469 (2020), 228397, https://doi.org/10.1016/j.jpowsour.2020.228397.

[19] K.E. Thomas-Alyea, M. Aryanpour, Design of composite electrodes with anion-absorbing active materials, J. Electrochem. Soc. 164 (2016) A6017, https://doi.org/10.1149/2.0021701jes.

[20] A. Vlad, J. Rolland, G. Hauffman, B. Ernould, J.-F. Gohy, Melt-polymerization of TEMPO methacrylates with nano carbons enables superior battery materials, ChemSusChem 8 (2015) 1692–1696, https://doi.org/10.1002/cssc.201500246.

[21] D.P. Abraham, S. Kawauchi, D.W. Dees, Modeling the impedance versus voltage characteristics of LiNi0.8Co0.15Al0.05O2, Electrochim. Acta 53 (2008) 2121–2129, https://doi.org/10.1016/j.electacta.2007.09.018.

[22] J. Landesfeind, H.A. Gasteiger, Temperature and concentration dependence of the ionic transport properties of lithium-ion battery electrolytes, J. Electrochem. Soc. 166 (2019) A3079–A3097, https://doi.org/10.1149/2.0571912jes.

[23] I.J. Ong, Double-layer capacitance in a dual lithium ion insertion cell, J. Electrochem. Soc. (1999) 4360, https://doi.org/10.1149/1.1392643.

[24] M. Park, X. Zhang, M. Chung, G.B. Less, A.M. Sastry, A review of conduction phenomena in Li-ion batteries, J. Power Sources (2010) 7904–7929, https://doi.org/10.1016/j.jpowsour.2010.06.060.

[25] T.L. Kirk, J. Evans, C.P. Please, S.J. Chapman, Modeling electrode heterogeneity in lithium-ion batteries: unimodal and bimodal particle-size distributions, SIAM J. Appl. Math. 82 (2022) 625–653, https://doi.org/10.1137/20m1344305s.

[26] A. Lasia, Impedance of Porous Electrodes. Electrochemical Impedance Spectroscopy and its Applications, Springer New York, New York, NY, 2014, pp. 203–250, https://doi.org/10.1007/978-1-4614-8933-7_9.

[27] B. Ravikumar, M. Mynam, B. Rai, Effect of salt concentration on properties of lithium ion battery electrolytes: a molecular dynamics study, J Phys Chem C Nanomater Interfaces 122 (2018) 8173–8181, https://doi.org/10.1021/acs.jpcc.8b02072.